Physics of cosmic rays

The term cosmic ray is used in the context of particles that travel through space close to the speed of light. Their kinetic energy far exceeds their rest mass, and ranges from $O(\text{GeV})$ for solar particles to energies exceeding 10^{20}eV for atoms of extragalactic origin. The latter are typically referred to as **U**ltra **H**igh **E**nergy CRs (UHECRs) in literature.

This chapter aims to introduce the general physical principles needed to describe cosmic rays. For this purpose, an overview of the origin of CRs is presented in **??**, discussions regarding their propagation in space, the resulting primary and energy composition are given in **??**, **??** and **??** respectively. Immediately following is a summary of the discovery of cosmic rays in **??**.

1 History

A first hint at the existance of high-energy particles in the upper atmosphere was given by Hess in 1912, who found that the discharge rate of an electroscope is altitude-dependant. Millikan coined the term cosmic "rays" for these particles, as he argued the ionizing radiation must be part of the electromagnetic spectrum [**millikan1928origin**]. This was later, at least partially, falsified with the discovery of the east-west effect [**johnson1938note**]. Hess' observation however withstood the tests of time and was ultimately recognized with the Nobel prize in physics in 1936 [**nobelprize1936**]. Two years later, in 1938, Pierre Auger showed via coincidence measurements that cosmic rays in fact originate from outer space, and gave a first description of extensive air showers [**auger1939extensive**]. Another 60 years later, the Pierre Auger collaboration would adopt his experimental setup and name in their search for cosmic rays of the highest energies.

In the meantime, numerous results from different cosmic ray detectors all over the globe have helped propel the related fields of particle physics, astro physics and cosmology to new insights. Observations from cosmic ray physics serve as a valuable cross-check to the hadronic interaction models developed e.g. at CERN [**ostapchenko2007status**]. New theories modeling the final moments in the life of stars have arisen thanks to results from e.g. Kamiokande [**goldman1988implications**]. Last but not least, publications by the Pierre Auger collaboration regarding the CR energy spectrum and flux help refine knowledge of our cosmic neighbourhood [**abraham2010measurement**, **aab2015searches**].

2 Acceleration

Following the detection of a cosmic ray on earth, the logically following questions are "where did it originate from?", and "how was it accelerated?". It is clear that particles with extreme energies must be created under extreme conditions. In particular regions with large **e**lectro**m**agnetic (EM) fields, either in field strength or spatial extent, play a big role in the acceleration of CRs for reasons listed in the following pages. Several acceleration mechanisms have been identified.

2.1 Diffusive shock acceleration (Fermi I)

Super **N**ova **R**emnants (SNR) typically feature a plasma sphere propagating outwards from the former stars core into the **I**nter **S**tellar **M**edium (ISM), in this region of plasma any magnetic field lines will be comoving, according to Alfvén's theorem [**alfven1942existence**]. First realised by Fermi, such SNR shock fronts serve as source of high-energy CRs [**fermi1949origin**].

If a low-energy particle is injected into the SNR shock front, it will eventually be reflected by the local $\vec{B}$-field. If the diffusion length within the plasma is much smaller than the spatial extent of the SNR, the shock front can be modelled as a plane, and the process is analogous to an elastic reflection against a wall. Consequently, if $\frac{d\vec{B}}{dt} = 0$, this does not cause the particle to gain any energy, espically because $W = \vec{F}_{\mathrm{L}} \cdot \vec{r} \propto (\vec{v} \times \vec{B}) \cdot \vec{r} = 0$. However, because the $\vec{B}$-field is moving radially outward alongside the plasma, a net energy gain of

$$\Delta E = +\beta_{\mathrm{SNR}} \cdot E_0 \tag{1}$$

arises, where $\beta_{\mathrm{SNR}} = |\vec{v}_{\mathrm{SNR}}| / c$ and E_0 are the velocity of the shock-front and the initial energy of the particle. From chapter 7 in [**fermi1949origin**] it follows that ionization losses within the shock front are not completely negligible. Hence a particle must have a sufficient energy such that ΔE in **??** exceeds possible ionization losses. The corresponding threshold for the primary energy above which acceleration occurs is dubbed the injection energy, and is of the order of 200 MeV for protons.

Furthermore, because typically $\beta_{\mathrm{SNR}} \leq 0.10$ a single acceleration cycle is not enough to explain the CR energies observed on earth. Instead, multiple cycles are needed. This requires additional, focusing $\vec{B}$-fields, provided for example by the ISM, which alter the trajectory of injected particles such that they can be reflected off the shock-front again.

With each cycle, the particles rigidity $R = |\vec{p}|c / q$ increases, until its gyroradius $\rho = R/|\vec{B}|$ exceeds the spatial extent of the focusing $\vec{B}$-field and the particle escapes into space. With an effective ejection probability p per cycle, the energy after n cycles and the expected flux w.r.t energy, $\Phi(E)$, becomes roughly

$$E(n) = E_0 \ (1 + \beta_{\mathrm{SNR}})^n . \tag{2}$$

$$N(n) = N_0 \ (1 - p)^n$$

$$\Leftrightarrow \quad \log\left(\frac{N(n)}{N_0}\right) = n \cdot \log\left(1 - p\right)$$

$$\Leftrightarrow \quad \overset{(??)}{=} \log\left(\frac{E(n)}{E_0}\right) \frac{\log(1-p)}{\log(1+\beta_{\mathrm{SNR}})}$$

$$\Leftrightarrow \quad N(E) = N_0 \cdot \left(\frac{E(n)}{E_0}\right)^{\log(1-p) \, / \, \log(1+\beta_{\mathrm{SNR}})}$$

$$\Rightarrow \quad \Phi(E) = \frac{\mathrm{d}N}{\mathrm{d}E} \propto E(n)^{\alpha-1}, \tag{3}$$

where $\alpha = \frac{\log(1-p)}{\log(1+\beta_{\mathrm{SNR}})}$ in **??** is a spectral coefficient whose exact value will depend on the age of the SNR (β_{SNR} decreases with age), the injected particle (different primaries have different injection energies and ejection probabilities), as well as many other factors that are often not known a priori. It can however be observed that the expected spectrum is a power law in the ranges from injection energy to a cutoff at the highest energies, which arises due to the finite lifetime of SNRs.

Results from several studies (e.g. [**aab2015searches**, **hillas2005can**, **blasi2013origin**]) hint that the presented first order Fermi acceleration mechanism is the main source of galactic CRs, extrasolar particles that originate from within the milky way, with energies ranging up to orders $O(\mathrm{TeV})$.

2.2 Stochastic scattering acceleration (Fermi II)

Second order (or stochastic) Fermi acceleration is the more general case of **??** and represents the original idea developed by Fermi in [**fermi1949origin**]. The underlaying principle of scattering particles off plasma clouds remains unchanged. However, if the diffusion length within the cloud exceeds its radius of curvature, the energy gain per collision instead becomes

$$\Delta E \propto + (\beta_{\mathrm{SNR}})^2 \cdot E_0. \tag{4}$$

Logically, this represents a much more inefficient acceleration mechanism, but is nevertheless observed in nature under certain circumstances (c.f. [**asano2015most**]).

2.3 Centrifugal acceleration in rotating $\vec{B}$-fields

Some astrophysical objects such as pulsars or **A**ctive **G**alactic **N**uclei (AGNs) possess strong magnetic fields ranging from $1\,\mathrm{T}$ for some AGNs [**daly2019black**] to $\approx 10\,\mathrm{GT}$ for magnetars, a subset of pulsars with extremely high magnetic flux densities [**flowers1977evolution**].

If such objects rotate at an angular velocity Ω, which is in general nonzero, charged particles at a radial distance r from the rotation axis will undergo centrifugal acceleration. In particular, their Lorentz factor γ behaves like **??** [**rieger1999particle**].

$$\gamma := \frac{E}{m_0 c^2} = \frac{\gamma_0}{1 - \left(\frac{\Omega r}{c}\right)^2},$$

(5)

where m_0 is the rest mass of the particle and γ_0 the prior Lorentz factor before acceleration. It follows that a test particle can in theory gain an arbitrarily high energy from this process by outspiraling towards the light cylinder surface, where $\Omega \cdot r = c$. In reality however, these processes are stopped by e.g. inverse Compton scattering at some point [**osmanov2007efficiency**]. In any case, [**rieger1999particle**] and [**osmanov2007efficiency**] conclude that values of $\gamma \approx 10^7 - 10^8$ are possible, corresponding to protons at $\approx 10\,\text{PeV} - 10\,\text{PeV}$ or iron nuclei at $\approx 500\,\text{PeV} - 5\,\text{EeV}$ energy.

2.4 Direct electrostatic acceleration

The presence of non-static $\vec{B}$-fields implies the existance of (in vacuum) comparably strong $\vec{E}$-fields and a corresponding electrical potential difference Φ across different regions within the magnetosphere. A back-of-the-envelope calculation reveals that they are (neglecting constant factors) proportional to

$$|\vec{E}| \propto \frac{\Omega\, r_0}{c} \cdot |\vec{B}|,$$

(6)

$$\Phi \propto r_0 \cdot |\vec{E}|,$$

(7)

where r_0 is the radius of the central object rotating at an angular frequency Ω. Consequently, an ion with atomic number Z can be accelerated to energies $E = Z \cdot e \cdot \Phi$, which can in some cases easily exceed 10^{20}eV [**rieger2009cosmic**].

Some caveats to this consideration need to be mentioned. Screening effects from plasma clouds surrounding the central body are expected to limit the electrical field strength, and maximum acceleration energy by extension. Additionally, losses via e.g. Bremsstrahlung have been neglected in the above calculation, limiting the maximum attainable energy in theory even further.

2.5 Other types & general classification

Several acceleration mechanisms have been discussed. A plethora of other interactions that are able to accelerate elementary particles to fantastic energies remain unmentioned, or even undiscovered, as CR physics is an active area of research. In general though the driving force behind all considered (and non-considered) acceleration mechanisms are
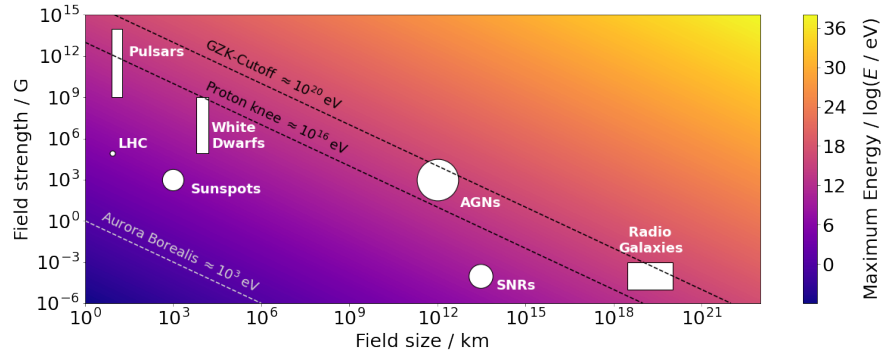
Figure 1: Rough estimate of field strength and size of different CR sources as well as the corresponding maximum energy estimated with **??** ($\beta = Z = 1$). Isoenergetic lines mark notable points in the energy spectrum discussed in **??**.

thought to be (electro-) magnetic fields, given their infinite range and large coupling strengths compared to other fundamental forces. Consequently, the maximum energy a specific CR accelerator with magnetic field $\vec{B}$ and size L moving at velocity βc can in theory provide for a particle with charge Ze is given by the Hillas formula [**hillas1984origin**]:

$$E_{\max} \, [\text{PeV}] = |\vec{B}| \, [\mu\text{G}] \cdot L \, [\text{pc}] \cdot Z \cdot \beta \tag{8}$$

This allows for an elegant classification of different cosmic ray sources, in part discussed on the previous pages, according to the Hillas plot shown in **??**.

2.6 Acceleration of uncharged particles

Particles like neutrons, neutrinos or photons possess no electromagnetic charge $q = 0$. Assuming **??** holds in these cases, they should thus not appear in the CR spectrum. This is in disagreement with reality, where energies from $100\,\text{GeV}$ up to $\approx 100\,\text{EeV}$ have been observed [**abeysekara2018very**, **ishihara2016extremely**]. Consequently, additional interaction channels are required to explain the existance of such uncharged CRs.

High energy γ-rays in particular can be created by accelerated, charged particles via Bremsstrahlung. This occurs for example during centrifugal acceleration near pulsars or AGNs (compare **??**). Furthermore, inverse Compton scattering with a high-energy cosmic ray can imply a significant energy gain for a photon [**jones1965inverse**].

Uncharged CRs are also frequently produced in nuclear interactions, such as e.g. deeply inelastic scattering of charged CRs with the ISM. This espically contributes to the CR photon spectrum, as high energy π^0 are often byproducts of such scattering processes. The uncharged pions then decay into two photons. Furthermore, neutrons or neutrinos can originate from interactions involving the weak force. When a proton converts to $p \rightarrow n + e^+ + \bar{\nu}_e$ during the dacy of a UHECR ion, the resulting decay products,

positron, neutron and electron-antineutrino inherit the parents' energy, and are thus high energy cosmic rays as well.

3 Propagation

Once a cosmic ray has been observed coming from some arrival direction (ϕ, θ), backtracking its' trajectory to an eventual origin is, ignoring external factors, in the literal sense, straight forward. It has been shown however that several effects need to be considered for an accurate treatment of CR propagation.

For uncharged CRs (γ, n), this task is simple. Such particles are not deflected by cosmic $\vec{E}$ and $\vec{B}$-fields. Possible interactions either demand the destruction of the particle (pair production, weak decay), or occur close to the source (e.g. Compton scattering), in which case the observed arrival direction will still be coincident with the actual source [**fermi201398**]. Gravitational lensing effects in some cases alter the trajectory of extragalactic photons. Such phenomena (if present in the first place) are however well understood in the scope of general relativity, and can be corrected for [**bartelmann2010gravitational**, **bartelmann2001weak**].

3.1 Intergalactic propagation & transport equation

Contrary, charged particles ($e^\pm$, p, ions) propagate along non-trivial paths within galaxies due to deflections from solar- and galactic EM-fields. While the galactic field is coherent over large scales, numerous irregular magnetic domains, seeded in part by individual stars complicate CR propagation to essentially a three-dimensional random walk [**haverkorn2015magnetic**]. It is thus challenging to pinpoint the origin of a charged cosmic ray.

Nevertheless, related queries, such as for example the question whether or not a particle of given energy is likely to be of extragalactic origin can be answered by examining the distribution of cosmic rays within a region of spacetime. The behaviour of a population of n_i particles of type i can be approximately recreated via the below transport equation:

$$\frac{\partial n_i}{\partial t} = \underbrace{Q_i}_{\text{Source}} + \underbrace{\nabla D_i\left(\nabla n_i\right)}_{\text{Diffusion}} - \underbrace{\frac{\partial k_i(E)}{\partial E}}_{\text{Energy}} - \underbrace{\left(\frac{n_i}{\tau_{\text{spal.},\,i}} - \sum_{j>i} \frac{n_j\, p_{ij}}{\tau_{\text{spal.},\,j}}\right)}_{\text{Spallation}} - \underbrace{\left(\frac{n_i}{\tau_{\text{rad.},\,i}} - \sum_{j>i} \frac{n_j\, d_{ij}}{\tau_{\text{rad.},\,j}}\right)}_{\text{Weak decay}}$$

- **Source** Q_i :

  The source term is responsible for the creation of CR particles (of type i). The exact form of Q_i will depend on the considered creation process. For example, the near instantaneous creation of n_γ photons in a **G**amma-**R**ay **B**urst (GRB) at time t_0 and location $\vec{r}_0$ can be modelled like $Q_\gamma = n_\gamma\, \delta(\vec{r} - \vec{r}_0)\, \delta(t - t_0)$.

- **Diffusion** $\nabla D_i (\nabla n_i)$:

  The random walk mentioned above is accounted for in the diffusion term, which takes a similar form to the Stokes-Einstein equation. The diffusion coefficient(s) D_i in the most general case take a tensor form due to anisotropic diffusion in different directions. Furthermore, D_i is different for each particle type, as the deflecting EM-fields couple to the respective charges q_i, which need not be equal in principle.

- **Energy loss** $\partial k_i(E) / \partial E$:

  During propagation, a cosmic ray can interact with the ISM, and lose energy in the process. If this happens often enough, the CR is eventually thermalized and does not contribute to the population i any longer. Different interaction channels for different CR types i require different loss models $k_i(E)$ for each type.

- **Spallation** $\left(n_i / \tau_{\text{spal.},i} - \sum n_j \, p_{ij} / \tau_{\text{spal.},j} \right)$:

  Nuclear spallation describes the process of violent disintegration of a target nucleus upon being struck by an energetic projectile. The resulting fragments can retain energies up to the projectiles energy. The spallation term in the transport equation considers both the destruction (first term), as well as creation (second term) of CRs i from heavier types j. It is assumed that spallation from type $j \rightarrow i$ occurs at a constant probability of p_{ij} in a characteristic time frame $\tau_{\text{spal.},j}$.

- **Weak decay** $\left(n_i / \tau_{\text{rad.},i} - \sum n_j \, d_{ij} / \tau_{\text{rad.},j} \right)$:

  If a particle j is weakly unstable ($\tau_{\text{rad.},i} < \infty$) there is a nonzero chance d_{ij} it decays into a daughter nuclei of some type i during propagation. The decay term reflects this and describes both decay from heavier and decay into lighter nuclei.

Insights to the physical implications of this parametrization can be gathered from a simplified example. Consider the case of a galaxy with height $2H$ and width W. It is $H \ll W$, and thus only diffusion along the $\pm z$-direction will be examined. Considering n_0 protons located at $z = 0$ initially, and ignoring interactions with the ISM, the transport equation reduces to the first two terms, with $D = (0, 0, D_z)^{\mathsf{T}}$ and $Q = n_0 \, \delta(z) \, \delta(t_0)$.

It can quickly be verified that a solution to the transport equation in this case is given by a normal distribution with mean $\mu = 0$ and standard deviation $\sigma = \sqrt{2D_z t}$. The diffusion coefficient D_z is a measure of how quickly the population spreads out (along the $\pm z$-direction). According to [**skilling1970diffusion**], D_z can be parametrized via the particles energy E_p, and characteristics of the present $\vec{B}$-fields.

$$D_z = \frac{1}{3} \frac{E_p}{m_p \, c^2} \cdot \frac{|\vec{B}| \cdot \langle L_{\vec{B}} \rangle}{\sqrt{\mu_0 \, \rho_{\text{ISM}}}}, \tag{9}$$

where $\langle L_{\vec{B}} \rangle$ is the characteristic length scale of deflecting $\vec{B}$-fields, μ_0 and ρ_{ISM} are the magnetic vacuum permeability and density of the interstellar medium respectively. After some time t, a fraction $r_{\text{esc.}}(t)$ of particles will have a z-coordinate $|z| > H$, and
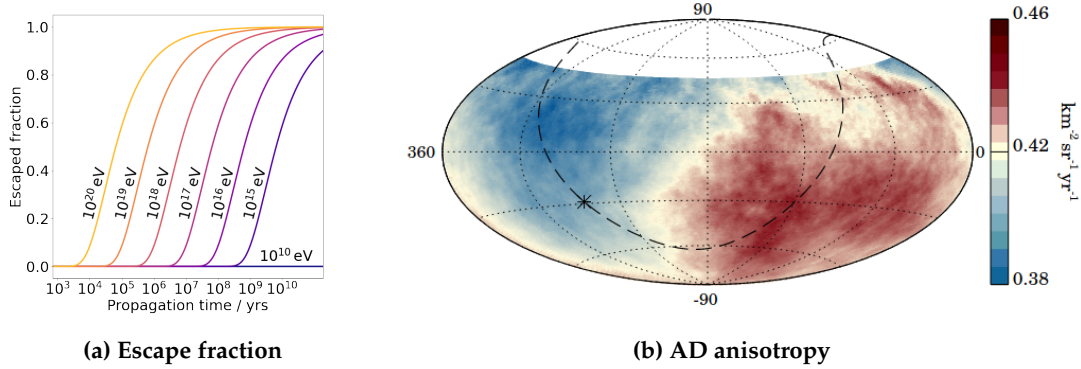
(a) Escape fraction

(b) AD anisotropy

Figure 2: (a) $r_{\text{esc.}}(t)$ according to **??** for protons of different energies.
(b) Dipole in the arrival direction of CRs with $E > 8\,\text{EeV}$. Image copied from
[**pierre2017observation**].

exit the disc consequently. In reality, this is not equivalent to the particle leaving
the galaxy, as large-scale halo structures extend above and below the visible disc
[**searle1978compositions**]. These halos are ignored here. $r_{\text{esc.}}(t)$ can thus be calculated
according to **??**. For some selected energies, a plot of the escaping ratio over time is
offered in **??**.

$$r_{\text{esc.}}(t) := 1 - \int_{-H}^{H} \frac{n(z,t)}{n_0} \, \mathrm{d}z \tag{10}$$

It can be concluded that low energy CRs do not travel outside their host galaxy within
reasonable timeframes. Meanwhile UHECRs with energies exceeding $E > 10^{18}\,\text{eV}$
escape swiftly on ballistic trajectories and are thus likely have an extragalactic origin,
not last also due to the limited energies that CR sources in the milky way can provide.

This observation is consistent with a dipole in the **A**rrival **D**irection (AD) of UHECRs
observed by the Pierre Auger observatory. The dipole points roughly in the opposite
direction of the galactic core, marked with an asterisk in **??**.

3.2 Extragalactic propagation & GZK-Cutoff

In the last paragraph the (likely) extragalactic origin of UHECRs was discussed. Such
particles must traverse millions of lightyears of extragalactic space before inducing a
large air shower on earth. As the energy of these primaries increases above the **G**reisen-
Zatsepin-**K**usmin threshold (GZK), their propagation through space is thought to be
severely impeded. At energies above $\approx 10^{20}\,\text{eV}$ the **C**osmic **M**icrowave **B**ackground
(CMB) consisting of photons in the microwave range are blueshifted to energies
$E_\gamma > 300\,\text{MeV}$. A proton with the corresponding energy can thus absorb such CMB
photons and convert to its' excited spin state, the Δ^+-baryon. The Δ^+-baryon decays

nearly instantanouely to (for example) the ground state again, by radiating away a π^0 and losing energy in the process [**PDG**].

The mean free path of this interaction, also labelled GZK horizon is both energy- and primary-dependant. For 75 EeV protons, it is ≈ 100 Mpc [**greisen1966end**]. Cosmic rays exceeding the GZK threshold should ergo not be observed from faraway sources, and an overall reduction in flux at these energies should be recorded [**zatsepin1966j**].

Indeed, results published by the Auger collaboration (see **??**) are consistent with this assumption. Whether or not the GZK-supression is the main cause for this soft spectrum at the highest energies remains unclear for now, but might be answered with the ongoing AugerPrime upgrade of the Pierre Auger observatory.

4 Composition

The composition of CRs largely mirror the relative abundances of elements in the universe with some noteable exceptions shown in **??**. Elements like beryllium (Be) or vanadium (V) are atypical products of supernovae and thus not as common as e.g. oxygen (O) [**gamezo2005three**, **cowan2004r**] in the solar system. This leads to a dip in the corresponding abundancy spectrum. The same dip is not observed in CR primary abundancies. While it is a priori existant upon creation of cosmic rays, it gradually gets "filled up" via e.g. spallation processes during their propagation until an equilibrium state is reached.

This equilibrium state depends sensitively on the characteristic age of cosmic rays, i.e. the mean travel time until a particle escapes the galaxy. Measuring CR composition hence enables the estimation of this parameter. Such an analysis is conducted in [**garcia1977age**], where it is found that the observed abundancies are consistent with a characteristic age of 1.7×10^7 yr for such high energy particles.

Contrary, hydrogen (H) and helium (He) are underrepresented (w.r.t their natural abundancy in the solar system) in cosmic ray particles. This is likely due to the comparably high ionization energy of both elements, which leads to less readily available hydrogen/helium ions. Since the acceleration mechanisms discussed in **??** all couple to the net charge q of a particle, unionized hydrogen and helium are not accelerated [**wang2002measurement**].

5 Energy spectrum

It has been discussed in **??** that the expected CR flux w.r.t energy for supernova remnants is a powerlaw in the rough range of 200 MeV $< E \lesssim 100$ TeV. Observations by various experiments extend this result to even higher energies. Their combined results are shown in **??**. However, while the general assumption of a powerlaw $\Phi(E) \propto E^\alpha$ holds over a large range of energies, kinks and other feature in the spectrum indicate that the spectral index α is not uniform, and instead a function of energy. The approximate
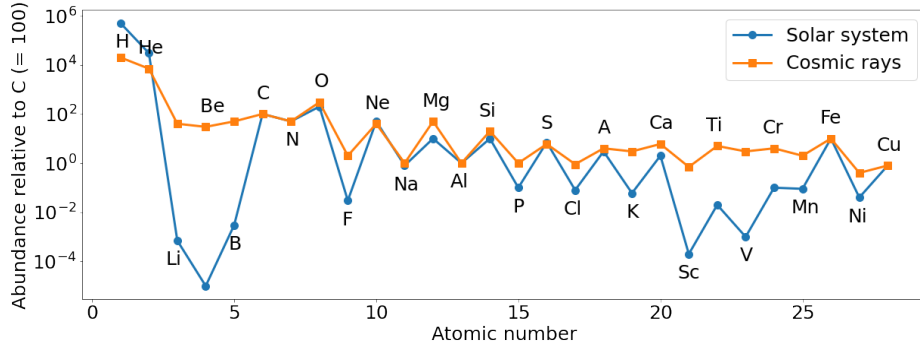
Figure 3: Composition expressed as abundancy relative to carbon for different sources. The ragged, alternating structure stems from an increased stability of nuclei with an even amount of protons (c.f. for example [**kirson2008mutual**]). Data from [**gaisser2016cosmic**]
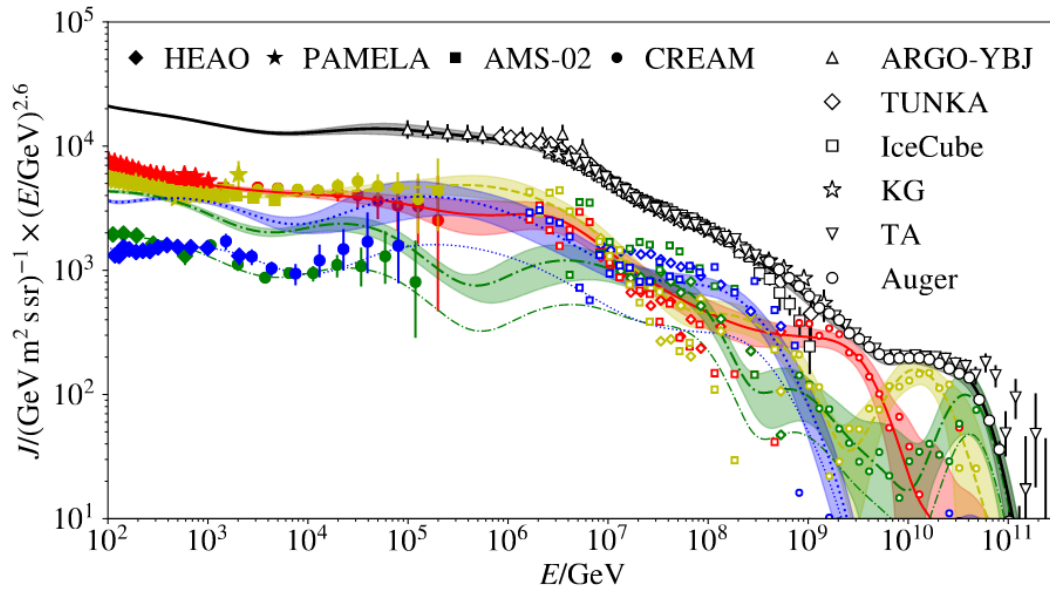

Figure 4: Measurements of the cosmic ray flux, multiplied by a factor $E^{2.6}$ for all types (black), and broken down by primary. Shown are protons (red), helium (yellow), oxygen (green) and iron (blue). Plot adopted from [**dembinski2017data**].

form of $\alpha(E)$ will be discussed in the following by examining several key regions of the energy spectrum.

- **Proton knee:**

  Below an energy of $\approx 1\,\text{PeV} = 10^6\,\text{GeV}$, it is $\alpha(E) \approx 2.7$, while above a spectral index of $\alpha(E) \approx 3.0$ is found [**gaisser2016cosmic**]. This softening of the spectrum (i.e. fewer particles of higher energy) could be attributed to several effects.

  - **Dark matter channel** (partially falsified)

    Weakly **I**nteractive **M**assive **P**articles (WIMPs) are a popular candidate for **D**ark **M**atter (DM), as they correctly estimate the cosmological evolution of the universe [**klypin1993structure**]. A WIMP with a sufficiently high mass could explain the kink in the energy spectrum. CRs with $E > m_{\text{WIMP}}c^2$ could in theory produce DM in deeply-inelastic scattering processes. The degree of steepening in the spectrum is a measure for how readily the process $X \rightarrow \text{WIMP} + Y$ occurs. The steeper the spectrum gets, the more particles are converted to DM, and the higher the corresponding cross sections are. Most theories involving WIMP creation can be excluded, since detectors at earthbound particle accelerators should have observed DM production at the observed steepening from 2.7 to 3.0 [**donato2009constraints**].

  - **Escape during propagation**

    While the analysis in **??** concludes that the escape time for $10^{15}\,\text{eV}$ protons to leave their host galaxy is at least of the order $10^8\,\text{yr}$ (compare **??**), the calculations leading to this result are extremely simplified. If a more accurate treatment finds that particles with rigidities corresponding to the relevant energies are no longer confined by galactic magnetic fields, the kink could originate from particles leaving the milky way and not contributing to the flux observed on earth any longer.

  - **Limited source energy**

    A last possible explanation might lie in **??**. A prevalent acceleration mechanism for CRs below 10^{15}eV, such as shock acceleration in SNRs for example, might not be able to provide energies exceeding this threshold due to physical constraints. The spectrum above the proton knee is thus populated by CRs that originate from different acceleration mechanisms with differen relations $\alpha(E)$.

- **Iron knee:**

  The spectrum exhibits various similar kinks at slightly higher energies than the one discussed in **??**, while it is assumed that they are ultimately caused by the same physical principles, each one corresponds to a different primary particle. Representatively, the iron knee at $E \approx 10^{17}\,\text{eV}$ is discussed here.

  Because iron has both a higher mass and charge ($Z = 26$, $A = 56$) compared to the proton ($Z = A = 1$), different processes couple to the different nuclei with

disparate strength. In particular, an iron core has a higher magnetic rigidity $R \propto \frac{A}{Z}$ than a proton of equivalent energy. This is explained by the fact that, while the iron core experiences a larger Lorentz force ($\propto Z$), the resulting acceleration ($\propto \frac{Z}{A}$) is not as strong due to a disproportionally larger mass ($\propto A$). It is thus logical to expect differences in the creation, propagation, and shower characteristics (see **??** for details) of different CR primary particles. By extension, the spectral index $\alpha(E)$ should be contrasting for each distinct particle type i, giving rise to different fluxes $\Phi(E)_i$, which is confirmed by **??**.

The ultimate cause of the different knees remains unknown currently. In the context of the ongoing AugerPrime upgrade, the Pierre Auger observatory will scan the energy spectrum at higher precision [**castellina2019augerprime**]. This will allow to test whether the location of the various kinks scale with A or with Z, and consequently shed light on the processes giving rise to these features.

- **Ankle:**

  At an energy of roughly $\approx 1\,\text{EeV} = 10^9\,\text{GeV}$ an inflection point is found, where the spectrum hardens again from an index $\alpha(E) = 3.0$ to ≈ 2.7. This might mark the final transition from predominantely galactic to intergalactic cosmic rays. If intergalactic CR sources such as AGNs have a harder spectrum (but lower luminosity) than galactic sources, the ankle could be well explained by a smooth transition from the latter to the former spectrum [**aloisio2007dip**]. Other explanations focus on a change of the primary composition, which seems to be apparent in **??** at the correct energy [**allard2012extragalactic**]. In any case, more data needs to be gathered to come to an informed conclusion on the ultimate cause.

- **Suppression:**

  At energies beyond $10^{20}\,\text{eV}$ a sharp drop in the flux can be noted. This represents the tail end of the spectrum, beyond which events are so rare that cosmic ray observatories can mostly just identify upper limits with their available statistics. The cause for the drop is actively debated, and might lie in the GZK cutoff discussed in **??**. Another explanation might be that the tail end represents the point at which even the largest and most powerful (in terms of energy) CR sources in the universe are not able to accelerate particles any further (c.f. **??**).

Extensive air showers

Extensive air showers describe the particle cascades that are the result of a high-energy cosmic ray interacting with the atmosphere of the earth. While the microstate of a given air shower is inherently chaotic, macroscopic variables such as the number of particles in the cascade, its' multiplicity, allow conclusions on the primary cosmic ray.

In this chapter the various processes which give raise to the jets of energetic particles are discussed. Because hadronic primaries that carry intrinsic SU(3)-color charges are fundamentally different from leptonic ones which do not, this is done in a two-fold way. The funamental principles giving rise to electromagnetic cascades are shown in **??**. Supplementary information regarding hadronic showers is listed in **??**. Finally, the effect of differing hadronic primaries is considered in **??**.

1 Electromagnetic showers

The dominating interaction of $E > 10\,\mathrm{MeV}$ photons in matter is e^+e^- pair production, whereas for electrons/positrons the creation of a γ via bremsstrahlung prevails at high energies. This is shown in **??**. Consequently, an entire cascade of $e^\pm$ and photons can emerge from a single primary particle, as realised by Heitler in [**heitler1984quantum**].

Of particular interest in these showers are, apart from the primary particles energy E_0 and arrival direction (Φ, θ), the atmospheric depth X_{max} at which it reaches its' maximum multiplicity, as well as the **L**ateral **D**istribution **F**unction (LDF), that parametrizes the distribution of particles along the shower axis. An important variable that influences both values is the radiation length X_0. It represents the characteristic length at which an $e^\pm$ loses $1 - \frac{1}{e} \approx 63\%$ of its energy. It also corresponds to the mean free path of a photon in matter up to a factor $7/9$ [**gupta2010calculation**]. Neglecting said factor and assuming that new particles on average inherit half of the parent energy, describing the multitude of particles contained in an electromagnetic shower becomes a counting exercise in the context of the Heitler-model.

With each radiation length, the number of particles N in the shower double, while the energy per particle E_{pp} halves. After traversing an atmospheric depth of $n \cdot X_{\mathrm{max}}$, typically measured in units of $\frac{\mathrm{g}}{\mathrm{cm}^2}$, they consequently read

$$N(n) = 2^n, \qquad E(n) = \frac{E_0}{2^n}. \tag{1}$$

After sufficient interactions, the energy of each individual particle E_{PP} will have degraded to such an extent that other processes are no longer negligible compared to

(a) γ interactions
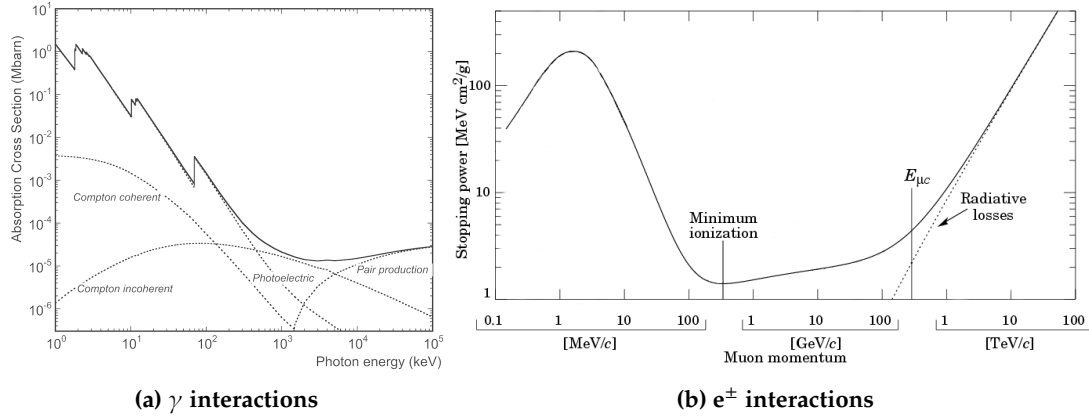

(b) $e^{\pm}$ interactions

Figure 1: (a) Cross section for different energy loss processes of a photon in tungsten. The sudden spikes correspond to the transition energy of increasingly higher-energy electron shells. From [**chen2007interactions**]. **(b)** Stopping power of copper, representatively on an antimuon μ^+, with respect to its' momentum. Plot adopted with changes from [**meroli2017straggling**].

bremsstrahlung and pair production. This occurs at the critical energy $E_{c,\,\mathrm{EM}}$ below which the shower rapidly stops creating new particles and dies out as a result. It follows via **??** and **??** that both $X_{\max}$ as well as $N_{\max}$ increase with E_0. The multiplicity arising from these assumptions alongside a stylized propagation of the thus created shower is represented in **??**.

$$E_{\mathrm{PP}}\left(n_{\max}\right) \overset{!}{=} E_c \overset{(\textbf{??})}{=} \frac{E_0}{2^{n_{\max}}}$$

$$\Leftrightarrow \qquad n_{\max} = \left\lfloor \log_2\left(\frac{E_0}{E_{c,\,\mathrm{EM}}}\right) \right\rfloor$$

$$\Rightarrow \qquad X_{\max} = n_{\max} \cdot X_0 = \left\lfloor \log_2\left(\frac{E_0}{E_{c,\,\mathrm{EM}}}\right) \right\rfloor. \tag{2}$$

$$\Rightarrow \qquad N_{\max} = 2^{n_{\max}} = \left\lfloor \frac{E_0}{E_{c,\,\mathrm{EM}}} \right\rfloor. \tag{3}$$

The number of particles at a given distance from the shower axis (y-axis in **??**) is essentially random, but follows a statistical basis, the lateral distribution function. The LDF can either be derived approximately from first principles [**kamata1958lateral**] or empirically, as is done in [**greisen1960cosmic**]. The latter arrives at a closed form approximation for the local density ρ of particles given a shower with multiplicity N at a distance r from the shower axis as

$$\rho_{\mathrm{EM}}(N, r) = \frac{0.4\,N}{r_{\mathrm{M}}^2} \left(\frac{r_{\mathrm{M}}}{r}\right)^{0.75} \left(\frac{r_{\mathrm{M}}}{r + r_{\mathrm{M}}}\right)^{3.25} \left(1 + \frac{r}{11.4\,r_{\mathrm{M}}}\right). \tag{4}$$
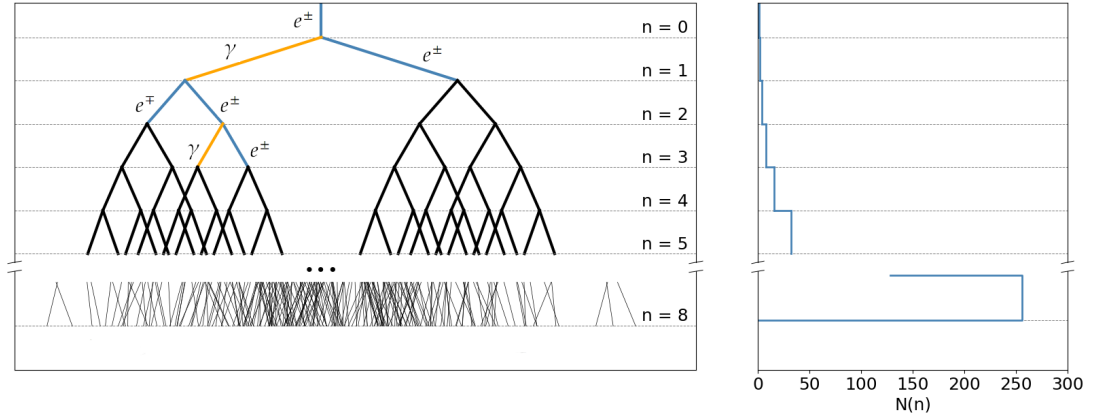
Figure 2: Shown on the left is the stylized propagation of an extensive air shower through the atmosphere according to the Heitler-model, quantized in units of X_0. The energy of the primary particle is of order $2^8 \cdot E_{c,\,\mathrm{EM}}$, which allows for 8 bifurcation steps, and $N_{\mathrm{max}} = 256$ shower particles. The multiplicity of the shower after each step is shown in the right subplot.

In **??**, the Molière radius r_{M} characterizes the lateral spread in multiple scattering processes. It is of order $r_{\mathrm{M}} \approx 100\,\mathrm{m}$ for interactions that are relevant here, and in general depends on the density of the considered material [**moliere1947theorie**].

2 Hadronic showers

Hadronic primaries will readily produce color-charged secondaries, as has been shown many times in particle accelerators. In order to model the development of hadronic showers, the model discussed in **??** thus needs to be adjusted. An example theory has been developed by Matthews in 2005. Following the reasoning in [**matthews2005heitler**], after traversing an atmospheric depth corresponding to the hadronic interaction length, a proton creates on average $N_\pi \approx 15$ pions, of which two thirds are charged, and one third is uncharged. The corresponding decay channels of the light π-mesons with the largest **B**ranching **R**atios (BR) are

$$\pi^+ \rightarrow \mu^+ + \nu_\mu \qquad (\mathrm{BR} \approx 0.9999,\ \tau = 2.6033 \times 10^{-8}\,\mathrm{s}\ [\mathbf{PDG}]),$$
$$\pi^- \rightarrow \mu + \bar{\nu}_\mu \qquad (\mathrm{BR} \approx 0.9999,\ \tau = 2.6033 \times 10^{-8}\,\mathrm{s}\ [\mathbf{PDG}]),$$
$$\pi^0 \rightarrow 2\gamma \qquad (\mathrm{BR} \approx 0.9882,\ \tau = 8.5 \times 10^{-17}\,\mathrm{s}\ [\mathbf{PDG}]).$$

With a mean lifetime of just attoseconds, the π^0 decay instantly before being able to continue the cascade process. In this fashion, the uncharged particles initiate a Heitler shower such as the one in **??**, by providing high-energy photons. It follows that every hadronic shower has an electromagnetic component. Moreover, assuming that the inherited energy from the parent particle is roughly uniformly distributed among its'

children, one third of the remaining energy in the hadronic component is lost to the electromagnetic component per hadronic interaction length.

Meanwhile, the charged pions repeat the procedure of creating secondary mesons, kicking off the hadronic component of the shower in the process.

Similar to the reasoning in **??**, a primary of given energy initiates a shower of a specific multiplicity $N_{\max}$. This is reached after $n_{\max}$ steps, where the energy per particle $E_{\mathrm{PP}}(n_{\max})$ is below the critical energy $E_{c,\,\mathrm{had.}}$ at which the mesons ionize rather than continue the cascade. After this last step, the charged pions eventually decay into muons and neutrinos. The shower characteristics are thus given by

$$
N_{\mathrm{had}}(n) = \left(\frac{2\,N_\pi}{3}\right)^n, \qquad E_{\mathrm{PP}}(n) = \frac{E_0}{N_\pi^n}, \qquad n_{\max} = \left\lfloor \log_N \left(\frac{E_0}{E_{c,\,\mathrm{had}}}\right) \right\rfloor, \tag{5}
$$

wheras the maximum multiplicity (ignoring neutrinos) in the shower is calculated as

$$
N_{\max,1} = \underbrace{\frac{3}{2}\left(\frac{2}{3}N_\pi\right)^{n_{\max}}}_{\text{Muon component}} + \underbrace{\sum_{k=1}^{n_{\max}-1} \frac{N(k)}{3} \cdot \left\lfloor \frac{E_{\mathrm{PP}}(k)}{E_{c,\,\mathrm{EM}}} \right\rfloor}_{\text{EM component}}. \tag{6}
$$

The muons stemming from pion decay follow a different LDF than the electromagnetic component. Again following the analysis in [**greisen1960cosmic**], the muonic LDF can be recovered as

$$
\rho_\mu(N,t) = 18 \left(\frac{N}{10^6 \cdot r}\right)^{\frac{3}{4}} \cdot \left(1 + \frac{r}{320}\right)^{-\frac{5}{2}}. \tag{7}
$$

While the above **??** drops off slower $O(r^{-\frac{3}{2}})$ compared to the electromagnetic component ($O(r^{-3})$), the immediate vicinity of the shower axis contains mostly photons and leptons from the EM subshower. Further out, the muonic component takes over. This is visualized in **??**. Due to this reason, and the fact that muons can carry considerable amounts of energy faraway from the shower axis, the muonic footprint of a shower often appears much more "patchy" compared to the EM portion. This knowledge is espically useful when distinguishing between hadron- and photon-induced air showers (compare [**capistran2015new**]).

3 Composite primaries

As is evident from the discussion in **??**, not only single protons (which are strictly speaking also composite) or elementary particles like photons, electrons, etc. appear in the cosmic ray spectrum. In theory, any somewhat stable particle is a possible primary.
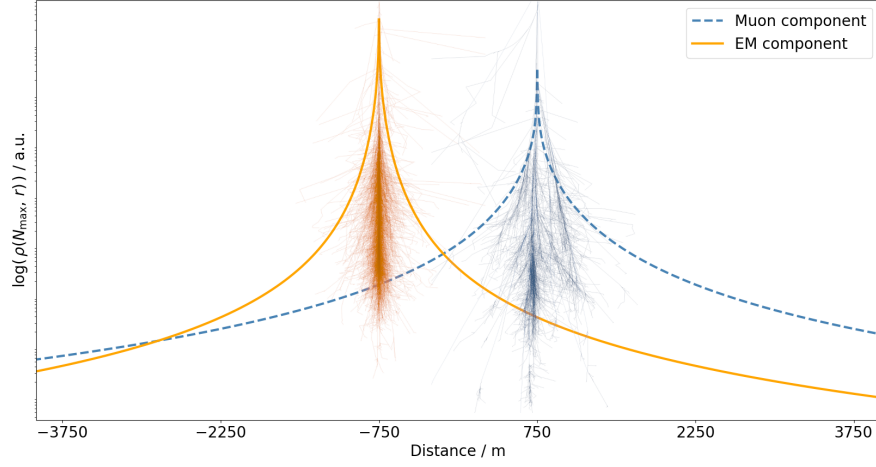
Figure 3: The lateral distribution function for the muonic (steelblue) and electromagnetic (orange) component of a vertical, 100 GeV proton shower at roughly sea level ($r_M = 100$ m). The inset plots on the top-right represent the xz-projection of the shower shape. Both images adopted with changes from [**CorsikaShower**].

The consequence of different primaries on resulting shower characteristics is subtle, but large enough such that it can be used for identification purposes.

Assuming the constituents in a CR nucleus all coherently interact with an air molecule, one arrives at the superposition principle for extensive air showers. It states that for a composite primary with $A = N + Z$ neutrons and protons, each constituent particle will initiate a subshower with initial energy of $E_0' = E_0 / A$, where E_0 is the initial energy of the composite particle. For this scenario, $N_{\max}$ and $n_{\max}$ are known from the preceding sections. It follows that air showers from heaver primaries occur at higher altitudes (lower atmospheric depth X) and with higher particle counts.

$$N_{\max, A} = A \cdot N_{\max}, \qquad n_{\max, A} = \left\lfloor \log_N \left(\frac{E_0}{E_{c, \text{had}}} \right) - \log_N A \right\rfloor, \tag{8}$$

where $N_{\max, A}$, $n_{\max, A}$ refer to the resulting extensive air shower characteristics that are induced by a particle with mass number A. On top of this, because more massive particles initiate more subshowers of comparably lower primary energy, and thus have lower $n_{\max}$, less energy is transferred from the hadronic to the electromagnetic shower component. This results in differing fractions of muonic to electromagnetic signal in the shower footprint.
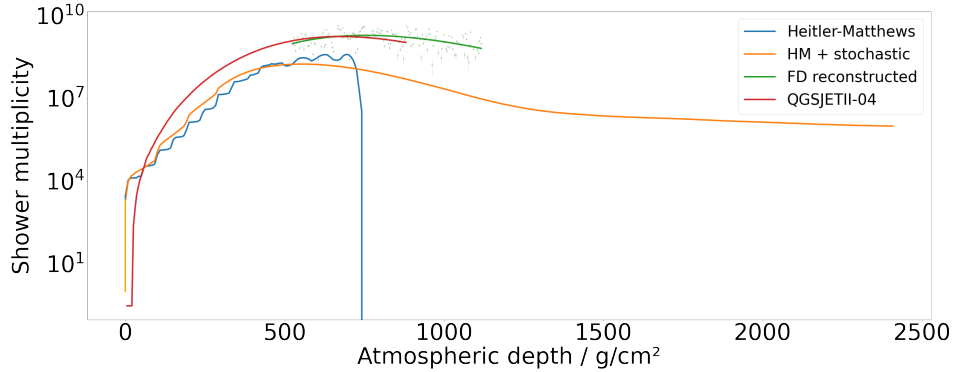
Figure 4: Comparison of the number of charged particles for different physics models to reconstructed observations from a 3 EeV proton shower. Shown in steelblue and orange is the Heitler-Matthews model as described in **??**, and extended with a stochastic component. An example of a more in-depth simulation in red, and observed shower multiplicities in green.

4 Comments on validity

The Heitler model and Heitler-Matthews model discussed in **??** and **??** respectively make only very rudimentary assumptions on the underlaying physics of particle cascades. Nevertheless, the equations recovered from these assumptions are already a close approximation of real world processes up to $X_{\max}$.

Of course, adding a stochastic component to the above assumptions (c.f. [**MartinShowerSim**]) improves predictions. But even full-fledged Monte-Carlo simulation software frameworks like GEANT4 [**agostinelli2003geant4**] or CORSIKA [**heck1998corsika**] show discrepancies between observed and predicted shower development when analysed in depth. This is shown in **??**.

While shower-to-shower fluctuations can explain discrepancies to a degree, there also exist systematic differences between the simulated and observed extensive air showers. These are largely owed to imprecise knowledge of the underlaying physical processes. For example, hadronic interaction models (e.g. QGSJETII-04) rely on extrapolation of measured cross sections in the GeV-TeV scales to the relevant CR energies [**ostapchenko2006qgsjet**]. While this is not an unfair assumption given the scale invariance of deep inelastic scattering [**fox1974early**], it is clear, that the approach cannot accurately encompass all effects that may take place at the high energies present in atmospheric particle cascades.

In conclusion, the particle cascades evolving from relativistic CRs impinging on earth are still not fully understood. Several simulation frameworks have been developed, which each have their own shortcomings. It is therefore important to compare not only results from simulations using one framework to observations, but also different simulations with each other.

5 Detection methods

5.1 Cherenkov light

When a charged particle exceeds the phase velocity of light in a medium with refractive index n, the optical equivalent of a sonic boom occurs. Photons travel in a shockwave along an angle $\theta = \arccos\left(n^{-1}\beta^{-1}\right)$ relative to the trajectory of the particle while $\beta \geq \frac{c}{n}$. This process is well understood and can be used to detect high energy cosmic rays.

Imaging Air Cherenkov Telescope

The refractive index of air ranges from 1 in the near vacuum of the upper atmosphere to $\approx 1 + 2.9 \cdot 10^{-4}$ at sea level [**andrews1992analytical**]. This implies that particles with a Lorentz factor $\gamma \gtrsim 41.5$ emit Cherenkov light, which is satisfied for e.g. muons and protons in the low GeV ranges and above.

It can therefore be expected that extensive air showers, which contain high energy charged particles, produce considerable amounts of Cherenkov light when propagating throught the atmosphere. This light, and by extension the air shower can be detected with **I**maging **A**ir **C**herenkov **T**elescopes (IACTs). Ground based experiments such as VERITAS [**VeritasTelescope**] or H.E.S.S [**HessTelescope**] detect gamma-rays using this technique.

Water Cherenkov Detector

The lightspeed in water is roughly 33% slower than in vacuum. Cherenkov radiation in water therefore occurs more easily than in air. Using this reasoning, a water tank equipped with means of detecting the emitted Cherenkov light, via e.g. **P**hoto**M**ultiplier **T**ubes (PMTs), should be able to measure traces of an air shower.

Indeed, this exact measurement principle of a **W**ater **C**herenkov **D**etector (WCD) was and is adopted in a variety of cosmic ray observatories such as the Pierre Auger observatory [**PierreAugerObservatory**], HAWC [**HAWC**], or Kamiokande [**Kamiokande**], for example.

5.2 Fluoresence

Ionization losses have been ignored in the discussion of the formation of extensive air showers. This is of course not completely accurate. During the development of an extensive air showers, particles excite, or even ionize the permeated medium. Consequently, spontaneous emission of photons due to recombination, or transition back to a ground state can be observed. The amount of fluorescence light produced in this way is a gauge for the number of particles present in the shower at a given moment.

In Air

The predominant element in air is nitrogen (78%), whose transitions lay in the UV-band [**FDReconstruction**]. After a nitrogen molecule is excited by a passing shower particle, a photon with wavelength $300\,\text{nm} \leq \lambda \leq 430\,\text{nm}$ is emitted isotropically due to relaxation. The low attenuation of ultraviolet radiation in air allows the fluorescence light to travel large distances before being absorbed [**elterman1968uv**]. This enables cameras like EUSO-TA [**abdellaoui2018euso**] or the **F**lourescence **D**etector (FD) of the Pierre Auger observatory (see [**FDReconstruction**] and **??**) to observe traces of extensive air showers from faraway during their development.

However, because of the low light yield of just $5\,\text{photons/MeV}$ [**nagano2004new**], the detectors must operate in low UV-noise conditions, which places an upper limit on their duty cycle.

In Scintillators

Conventional plastic scintillators have a light yield, that is $1000 - 10000$ times higher than that of air [**holl1988measurement**]. Such scintillators therefore pose an effective way of measuring a shower footprint on the ground. The Pierre Auger **S**urface **D**etector (SD) is equipped with scintillators during the ongoing AugerPrime upgrade. Predecessors like KASCADE [**Kascade**] have been using scintillation light to detect cosmic rays as well.

5.3 Radio Emission

Relativistic charged particles in the cascade are subject to deflections due to the geomagnetic field. This deflection is largest for $e^{\pm}$ due to their comparably tiny masses. Albeit the deflection of a typical electron in the shower is miniscule and the subsequent emission of Bremsstrahlung tiny, coherence effects along the entire shower front can greatly amplify the electric field strengths obtained from this effect [**aab2018observation**]. This gives rise to radio signals emitted by the extensive air shower, which can in principle be detected via antennas.

One challenge in constructing an efficient CR radio detector is the requirement for a radio-quiet environment, where a large enough **S**ignal-to-**N**oise-**R**atio (SNR) permits analysis of measured data. This is the case for the AERA component of the Pierre Auger observatory, which has been in operation since 2010 [**Aera**]. Its results have in part lead the proposal of a vast radio array, GRAND [**Grand**], which will have an enormous exposure to CR showers, if built.

The Pierre Auger Observatory

Located on the argentinian high-plains of Pampa Amarilla, the Pierre Auger observatory is a hybrid detector designed to detect and study cosmic rays of the highest energies. With an effective area of $3000\,\text{km}^2$ it is by far the largest experiment of its kind [**DesignReport**].

Altough first proposed in 1992, it took 18 years until the idea of a large scale experiment to detect cosmic rays matured and construction of the first prototype started near Mendoza [**AugerTimeline**]. Some further 20 years later, the Pierre Auger collaboration has co-authored over publications and continues to advance research in astroparticle physics.

It does this via a hybrid approach, combining measurements of a **S**urface **D**etector (SD) as well as a **Fl**ouresence **D**etector (FD). Additional machinery, such as the e**X**treme (XLF) and **C**entral **L**aser **F**acility (CLF), is installed to monitor atmospheric variables. This improves the overall systematic accuracy of predictions made by the experiment. An overview of the site can be seen in **??**. Data measured by the FD, SD and the atmospheric monitors is sent to a **C**entral **D**ata **A**cquisition **S**ystem (CDAS) located in the nearby town of Malargüe.

This chapter offers a brief look into the measurement principle and setup of the observatory. Information regarding the fluoresence detector can be found in **??**. The SD is described in **??**. A more in depth read on detector specifications and design choices is represented by the Pierre Auger observatory design report [**DesignReport**], where a lot of information stated in this chapter is conglomerated from. Notes on the event reconstruction are listed in **??** and summarized from [**SDReconstruction**] and [**FDReconstruction**].

1 Fluoresence Detector (FD)

The FD consists of a total of 27 fluoresence telescopes (eyes) at 4 different sites. Each eye monitors a 30° x 30° window of the sky at a resolution of $\approx 0.5\,\frac{\text{px}}{\text{deg}^2}$. This results in an effective FOV of roughly 180° x 30° per FD station, with an exception of Coihueco, where three additional telescopes - HEAT (**H**igh **E**levation **A**uger **T**elescope) - are installed to enable monitoring of higher zenith angles ($30° \leq \theta \leq 60°$) and increase sensitivity for showers of lower energies (compare **??**). A schematic of the setup of each eye is given in **??**.

The individual telescopes consist of 3.6 m by 3.6 m, convex mirrors. They reflect incoming light onto a set of 440 photomultipliers (PMTs), each corresponding to one
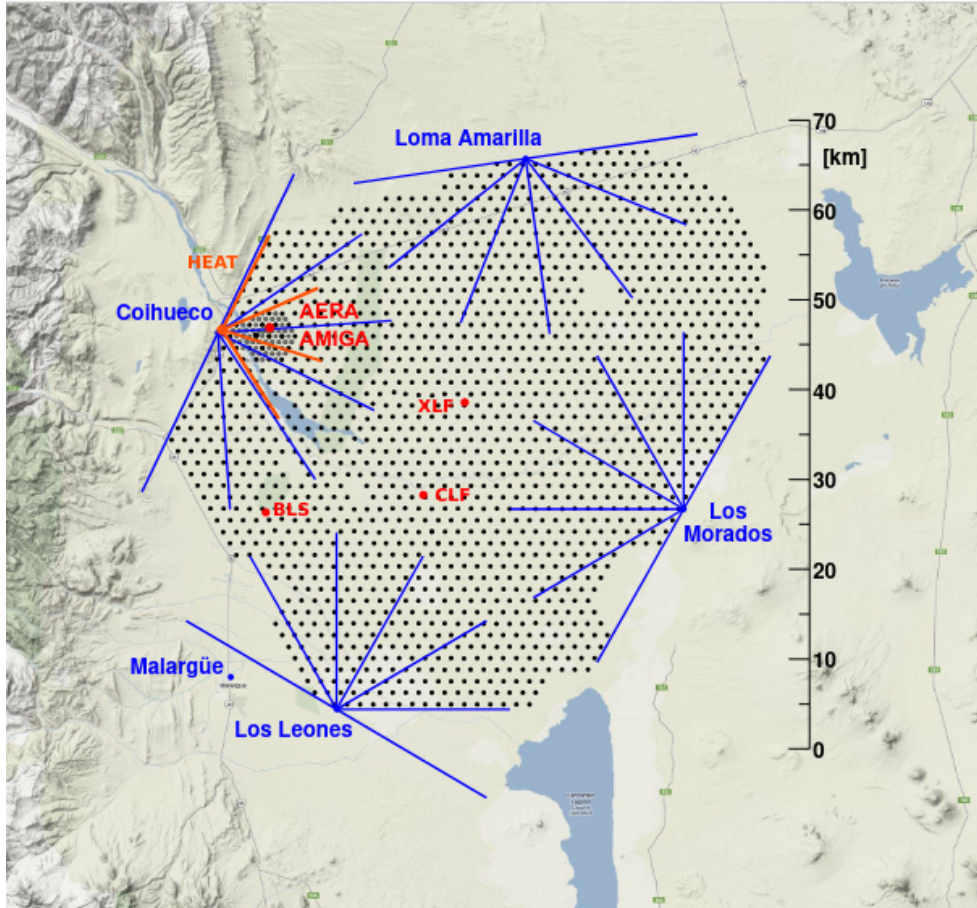
Figure 1: Overview of the Pierre Auger observatory. The four different FD sites (respective FOV shown with blue lines) sit at the edge of the detector area and monitor the night sky above the SD array consisting of 1600 water tanks (black dots). A denser spacing of stations near Coihueco is equipped with additional electronics such as e.g. radio antennas (AERA) and muon detectors (AMIGA). Image taken from [**AugerArray**]
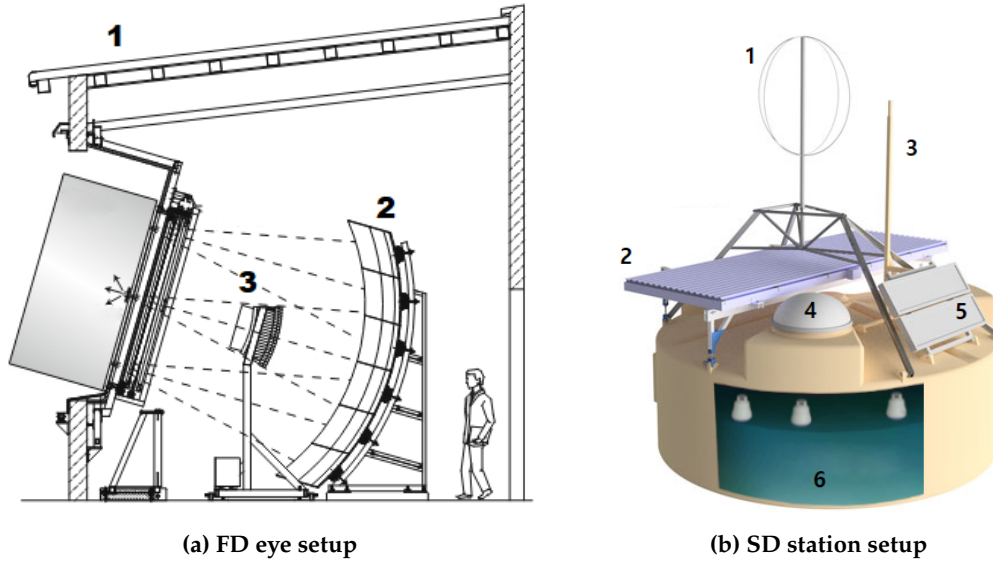
.

(a) FD eye setup   **(b) SD station setup**

Figure 2: (a) Schematic view of an FD eye with housing (1), main mirror (2) and camera (3). Image taken from [**FDReconstruction**] **(b)** Setup of an SD WCD with radio antenna (1), SSD (2), communication and GPS antenna (3), electronics box (4), solar panesl (5) and the WCD (6). Image adopted with changes from [**UUBstation**] and [**waterTank**]

pixel in the resulting image seen by an eye. Since the setup needs to be extremely sensitive to UV light in order to detect flouresence caused by extensive air showers, its operation is limited to the relatively noise free moonless astronomical nights (Sun $\angle$ Horizon $\lesssim -18°$). When the FD is operational, this allows the observation of the longitudinal propagation of a shower instead of just its' footprint (as seen by the SD).

2 Surface Detector (SD)

The SD consists of 1600 individually operating stations, spaced apart on a hexagonal grid with a standard 1.5 km spacing. Each station is made up of a main tank filled with 12 000 L of purified water and reflective inner walls, a solar panel and batteries for power management, as well as an antenna for communication. Within each tank three PMTs detect Cherenkov light originating from shower particles, these are together with the tank referred to as **W**ater **C**herenkov **D**etectors (WCDs). With the (at the time of this work) ongoing AugerPrime upgrade, each station is additionally equipped with a **s**mall **PMT** (sPMT), **S**urface **S**cintillator **D**etector (SSD), and radio antenna atop the tank. This allows for the recording of stronger signals, finer separation of electromagnetic and muonic shower component and detection of highly inclined air showers respectively [**AugerPrime**, **horandel2019precision**]. **??** shows a schematic blueprint of each SD station.

2.1 Data acquisition (DAQ)

Onboard electronics, the **U**pgraded **U**nified **B**oard (UUB), or more precisely six 10-bit **F**lash **A**nalog-to-**D**igital-**C**onverters (FADCs) read out measurement data from the PMTs at a sampling rate of 120 MHz ($\approx$ 8.33 ns binning) [**verzi2013energy**]. This is done in a two-fold way. Three FADCs digitize the PMTs dynode voltage, resulting in the **H**igh **G**ain (HG) output. Three FADCs monitor the anode voltage to form the **L**ow **G**ain (LG) output, which can be analyzed if the HG output exceeds a value of 2^{10} ADC counts and becomes saturated. This effectively enables the measurement of both large ($\geq O(10^3)$ particles hitting the tank) as well as small shower signals ($O(1)$ particle hitting the tank) with sufficient accuracy [**SDReconstruction**]. Once an FADC bin has been recorded and checked for possible triggers (c.f. **??**) it is written to a ring buffer. If a trigger is issued, the corresponding chunk in the ring buffer ($\approx$ 4.992 μs (599 bins) before and 12.07 μs (1448 bins) after a trigger, 2047 + 1 bins total), the measured trace, can be analyzed in order to calibrate a station in the array (**??, ??**) or processed by a higher-level CPU for event reconstruction purposes (see **??**).

While each station is equipped with the same electronics and runs the same analysis software, variables like the position in the field, station age or slight changes in the manufacturing/installation process cause different stations to age differently. Over the lifetime of the array such differences can sum into potentially drastic discrepancies in gathered data. Put simply, an extensive air shower will look different both to different WCDs at the same time as well as the same WCD at different times. To account for this, measurements are standardized across all stations. ADC counts are related to a **V**ertical **E**quivalent of through-going **M**uons (VEM) that would result in the same signal strength. In this fashion, the maximum response that is generated by a PMT from one vertically through-going muon is defined as 1 VEM$_{\text{Peak}}$. The total deposited charge (equivalent to the integral of the response) is defined as 1 VEM$_{\text{Ch.}}$. The conversion factor between ADC counts and VEM$_{\text{Peak}}$ and VEM$_{\text{Ch.}}$ (referred to as I_{VEM} and Q_{VEM} respectively) is estimated from data and continuously updated separately for each station. Note that due to the limited computational resources of the WCD, as well as constraints on the amount of data that can be transmitted per station in the SD array ($1200 \frac{\text{bit}}{\text{s}}$, [**localStationCalib**]), a simplified, rate-based approach is implemented for autonomous calibration in the field (Online calibration), this stands in contrast to the more physics-driven histogram method used during event reconstruction (Offline calibration). In any case, both algorithms are listed in the following subsections and discussed in more detail in the referenced literature.

2.2 Offline calibration

Baseline estimation

In order to estimate I_{VEM} and Q_{VEM} of a WCD tank first the baseline - the average response in the absence of any signals - of each PMT needs to be determined. All further analysis will then be based on the baseline-subtracted PMT data.

For event reconstruction, a first baseline estimate of a WCD PMT is predicted by examining the beginning and end of a 2048 bin (17.06 µs) long trace. The mode m as well as standard deviation σ of the first (last) 300 bins is calculated. All bins larger or smaller than $m \pm 2\sigma$ are truncated and removed from the trace window. The value of m, σ is consequently updated and the procedure repeated until a convergence is reached and no further cut is necessary. The best estimate B_{front} (B_{end}) for the front (end) of the trace at this point is given by the mean value of all remaining bins. It's statistic uncertainty $\sigma_{B_{\mathrm{front}}}$ ($\sigma_{B_{\mathrm{end}}}$) is given by the standard deviation of the remaining bins [**tobiasBaseline**]. The baseline between the flat front and end estimate is then interpolated based on the difference

$$\Delta B = B_{\mathrm{end}} - B_{\mathrm{front}}. \tag{1}$$

- **Rejection of anomalous upward fluctuations $\frac{\Delta \mathbf{B}}{\sigma_{\Delta \mathbf{B}}} \geq +10$:**

  B_{end} being higher than B_{front} often indicates errors in the electronic readout or defect components in the measurement chain. There exists no physical reason why the end baseline should be (significantly) higher than the front. Consequently, traces where this is the case are ignored during event reconstruction.

- **Constant approximation for small upward fluctuations $+5 > \frac{\Delta \mathbf{B}}{\sigma_{\Delta \mathbf{B}}} \geq 0$:**

  Small fluctuations of the baseline are expected and the norm. If these fluctuations are positive ($B_{\mathrm{end}} > B_{\mathrm{front}}$) the method of calculating the mode, truncating outliers and repeating both steps is applied to the entire length of the signal, resulting in a constant baseline estimate B across the trace.

- **Step-function approximation for small downward fluctuations $0 > \frac{\Delta \mathbf{B}}{\sigma_{\Delta \mathbf{B}}} \geq -1$:**

  Unlike positive fluctuations, negative fluctuations ($B_{\mathrm{end}} < B_{\mathrm{front}}$) can have a physical significance. Due to the undershoof of PMTs after detecting a signal in the WCD (compare [**glietta2008recovery**]), the baseline estimate decreasing towards the end of the trace often indicates the presence of shower particles within the tank. For this reason, downward fluctuations are handled differently from upward ones. If the fluctuations are sufficiently small, the baseline across the trace is estimated as a simple step-function; The trace is separated into two parts along its' maximum ADC value. The front part (i.e. before the max. value) has the baseline B_{front}, while the rear part is estimated by B_{end}. An example of this is shown in **??**.

- **Charge-linear approximation for large undershoots $-1 \geq \frac{\Delta \mathbf{B}}{\sigma_{\Delta \mathbf{B}}}$:**

  For larger undershoots, the baseline is estimated bin by bin based on the deposited charge in the detector. Starting with a value of B_{front} for the bins 1-300, the remaining baseline is first linearly interpolated according to **??**,

$$b_i = B_{\mathrm{front}} - \Delta B \cdot \frac{i - 300}{1448}, \qquad 300 \geq i \geq 2048, \tag{2}$$

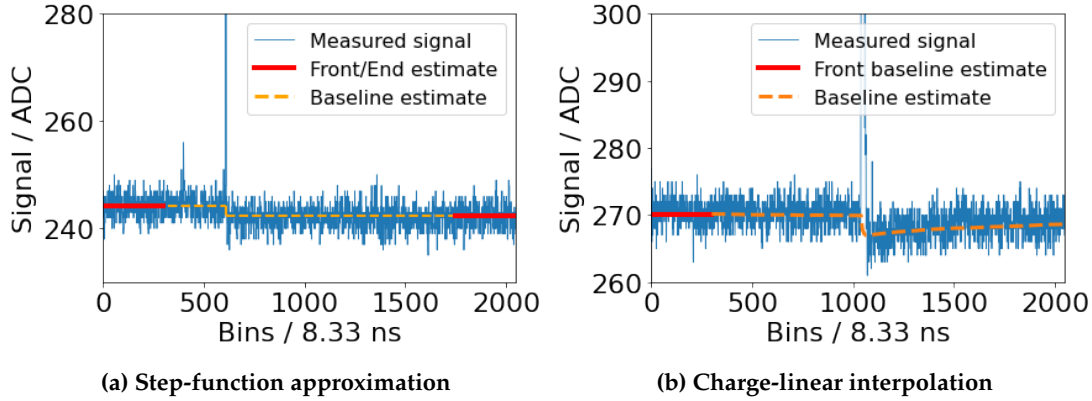(a) Step-function approximation   (b) Charge-linear interpolation

Figure 3: **(a)** A simple step function is sufficient to accurately model a PMTs' noise level at small downward fluctuations. **(b)** For larger discrepancies the more involved charge-linear interpolation is used. Note that the signal undershoot is exaggerated for visualization purposes in both examples.

where the magic numbers 300 and 1448 refer to the last bin of the front baseline estimate and the length of the interpolated baseline respectively. From this, the deposited charge q_i up to bin i can be calculated as per **??**.

$$q_i = \sum_{k=0}^{i} (T_k - b_k) \exp\left(-\frac{8.33\,\text{ns}}{\tau} \cdot (i - k)\right) \tag{3}$$

In **??**, T_k refers to the numerical value of bin k. Note that an exponential falloff term has to be added to account for the decay in signal undershoot with a decay time of $\tau = 45\,\mu\text{s}$. The value of τ is determined in [**tobiasBaselineUUB**]. Assuming the magnitude of the signal undershoot is directly proportional to the deposited charge q, a correction of the baseline thus becomes

$$b_i = B_{\text{front}} + \frac{q_i}{q_{1898}} \cdot \Delta B. \tag{4}$$

The parametrization in **??** is chosen such that the charge-interpolated baseline at bin 1898 (the center position in the last 300 bins) is exactly equal to the rear baseline estimate B_{end}. The prediction can be made more accurate by repeating the above steps, each time recalculating q_i and readjusting the baseline b_i in the process. **??** shows an example baseline estimate after three such iterations. In general, it converges to a robust estimate within five repetitions [**tobiasBaselineUUB**].

Estimation of I_{VEM} and Q_{VEM}

The conversion factor between ADC counts and VEM$_{\text{Peak}}$, VEM$_{\text{Ch.}}$ are built from distributions of traces that satisfy the muon trigger, which scans incoming ADC bins for a value exceeding the muon threshold $t_\mu = b + 30\,\text{ADC}$, 30 ADC above baseline, for
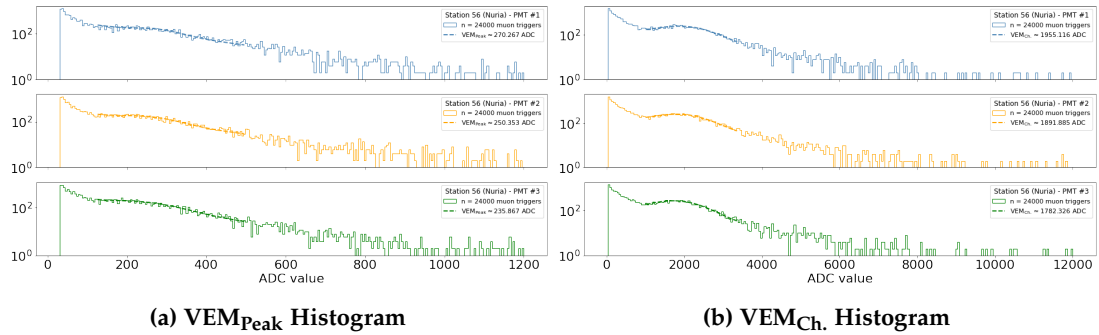
(a) VEM$_{\text{Peak}}$ Histogram   (b) VEM$_{\text{Ch.}}$ Histogram

Figure 4: (a) The maximum value of each muon trace is histogrammed in order to gain information about the current value of I_{VEM} of a station. **(b)** The conversion factor from recorded ADC values to Q_{VEM} is given from the histogrammed sum of each muon trace.

any of the three WCD PMTs. If this requirement is met, 69 bins (19 before, trigger bin, 49 after) are written to the muon buffer, a FIFO (first-in-first-out) type memory storage, that is subsequently filled with low-energy events, which (in general) didn't satisfy any other trigger but still contain useful information [**localStationCalib**].

By histogramming the maximum value (sum) of each trace, the plot shown in **??** (**??**) can be obtained. It becomes apparent that the number of events per bin largely follows a power law with negative spectral index. This is expected considering the discussion in **??**. Noteable are characteristic deviations from this powerlaw, as these contain information about I_{VEM} and Q_{VEM} :

- Low energy events from e.g. e^-, e^+ that deposit their entire energy in the tank give rise to a surplus of events at lower ADC values.

- A characteristic (muon) hump appears in the bins $20-70$. This surplus is caused by omni-directional muons impinging onto the detector. Since the energy deposited by such muons is roughly constant, the center of the muon hump serves as an estimate of I_{VEM} (Q_{VEM}).

- (Not depicted in **??**) In similar plots from related works (c.f. [**localStationCalib**, **streich2018performance**]) a drastic increase in bin occupations towards the tail end of the histograms can be observed. This is attributed to an increased bin size from 1500 ADC counts onwards, which reduces the amount of data per station sent to CDAS. In the example plots referenced here, a constant binning is chosen instead. This difference is mentioned here to avoid possible confusion.

In this fashion, the average response of the WCD to a through-going muon can be estimated by e.g. fitting a gaussian distribution to the muon hump. However, there exists a systematic difference between the response to a vertical or an omni-directional muon. Consequently, correctional factors need to be applied to the analysis results. These have been determined in previous experiments [**allison2002surface**]. Finally, one arrives at an estimate for the conversion factor between ADC counts and VEM$_{\text{Peak}}$, VEM$_{\text{Ch.}}$.

2.3 Online calibration

Baseline estimation

Each SD station has an autonomous estimate of its' three WCD PMT baselines. They are defined simply as the mean of all first bins for each trace contained in the respective muon buffers (see **??**). This baseline estimate is used to set the thresholds of the hardware triggers discussed in **??**.

Estimation of I_{VEM} and Q_{VEM}

Due to the limited computational resources in each station, the determination of I_{VEM} and Q_{VEM} at station-level is fairly naive. Nevertheless, the σ-δ-method shown here has proven to be incredibly robust over the lifetime of the SD array [**DesignReport**].

In the beginning, the to-be-estimated value $I_{Peak}^{est.}$ ($Q_{Peak}^{est.}$) is set to the same, predefined value for all PMTs. A simple single-bin calibration trigger requiring all available WCD PMTs to be above a threshold of $t_{70} = 1.75\,I_{Peak}^{est.}$ above baseline plus a given PMT exceeding $2.5\,I_{Peak}^{est.}$ is used to determine a calibration trigger rate. If for some reason not all three WCD PMTs are functional, the thresholds are altered according to **??**. What follows is an iterative procedure to approximate I_{VEM} (Q_{VEM}):

1. Calculate the trigger rate $r_{cal.}$ of the calibration trigger over a time $t_{cal.} = 5\,\mathrm{s}$.

2. Adjust $I_{Peak}^{est.}$ ($Q_{Peak}^{est.}$) by $\pm\delta$ if $\pm(r_{cal.} - 70\,\mathrm{Hz}) \geq 2\,\mathrm{Hz}$, with $\delta = 1\,\mathrm{ADC}$ initially.

3. If $t_{cal.} < 60\,\mathrm{s}$ increase $t_{cal.}$ by $5\,\mathrm{s}$. If $\delta > 0.1\,\mathrm{ADC}$ decrease δ by $0.1\,\mathrm{ADC}$.

4. While $t_{cal.} < 60\,\mathrm{s}$ jump to step 1, else return $I_{Peak}^{est.}$ ($Q_{Peak}^{est.}$).

Table 1

n_{PMT}	t_{70}
1	2.85
2	2.00
3	1.75

3 Event Reconstruction

If an event has been detected (**??**) it is reconstructed at CDAS level, where information from all relevant detectors is conglomerated. From the observed shower footprint in the SD array as well as the (if available) longitudinal profile measured by the FD stations follows an estimate on arrival direction (**??**), energy (**??**) and primary particle
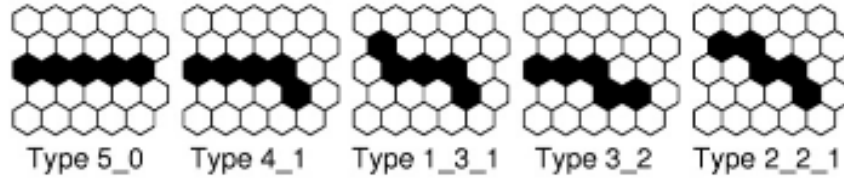
Figure 5: Fundamental shape of tracks considered straight. Image from [**FDReconstruction**].

(**??**). As the work presented in this thesis solely deals with the surface detector of the Auger observatory, this section focuses heavily on the SD reconstruction. Addendums towards FD reconstruction are given where needed.

3.1 Trigger procedure

The flux of cosmic rays espically at the highest energies is barely of the order of $1\,\mathrm{km}^{-2}\,\mathrm{yr}^{-1}$ [**hillas1984origin**]. Consequently, most signals observed by the Auger observatory stem from low-energy cosmic muons and not extensive air showers. This is reflected in the hierarchical structure of the triggers, which effectively reject such events. The overall event detection is split up into three tiers, T1, T2 and T3, where T3 implies the detection of an extensive air shower by either the FD or the SD (or both).

T1 trigger

T1 level triggers are implemented at the lowest possible level. This means each FD eye or each SD station raises T1 triggers autonomously. They serve as a first indicator on whether or not a signal of any kind is present. For the most part, this is realised by checking for elevated signal strengths, i.e. for hot pixels in a FD telescopes image or PMT outputs of an SD station that are significantly above baseline. The respective trigger thresholds are calibrated such that the nominal trigger rate during operation is roughly 100 Hz [**FDReconstruction**, **SDReconstruction**].

T2 trigger

T2 level triggers occur at the same location as T1-type triggers. They are different in their more stringent conditions on the signal size or shape. This for example entails track shape identification for the FD telescopes, where straight tracks (see **??**) of hot pixels are identified. If the resulting pixel track passes an additional quality cut that rejects e.g. lightning signals, the T2 is directly promoted to a T3 trigger (= Event). For the SD, an exact discussion of T2 triggers is given in **??**. A single tank on average records T2-type events at a rate of 20 Hz and forwards this information to the CDAS along with a timestamp. There, incoming information of all tanks is scanned for spatial and temporal correlations, which indicate the presence of an extensive air shower.

T3 trigger

T3 type triggers, or event type triggers are (with the exception of FD events, which have been discussed above) built from distributions of at least three SD stations next to each other that recorded a T2 trigger in close temporal succession. Upon the detection of such a pattern a readout command is issued to all nearby stations. Their recorded FADC traces as well as calibration information are forwarded to CDAS if the station observed a T1/T2 event within an appropriate timespan of order $O(\mu s)$ before or after the T3 pattern occurence. Such a modus operandi enables an accurate reconstruction of the shower footprint by including stations that did not participate in the initial T3 trigger. This extends to FD issued T3 triggers, where potential information from SD stations in the vicinity of the FD-reconstructed shower core position is requested.

3.2 Core position

All reconstruction algorithms presented in the following subsections rely in one form or the other on an accurate determination of where the shower was recorded above the observatory. Hence the center of the shower footprint, the shower core, must be estimated at the beginning of the analysis chain.

Without any prior knowledge, a first guess as to where the shower core is located can be made by calculating the barycenter of all participating stations. In this fashion, a weighted mean of all station locations is constructed with weights equal to the square root of the corresponding signal strength [**SDReconstruction**].

The presented approach fails if only parts of the shower are contained within the SD event. This occurs espically at the edges of the SD array, or in the vicinity of faulty WCDs. A fiducial trigger, $NT5$, is employed to mitigate this problem. $NT5$ requires at least N active stations around the SD detector that recorded the largest signal [**abraham2010trigger**].

3.3 Arrival direction

The shower footprint measured by the SD (example given in **??**) corresponds to the projection of the shower plane onto the detector plane, i.e. the ground. It can be assumed that the shower plane has a fixed (hyperbolic [**bonifazi2005angular**]) shape and propagates at the speed of light along the primary particles trajectory. With this knowledge, estimating the arrival direction becomes a task of minimizing the difference between measured and expected arrival times given by an example shower axis anchored at the reconstructed shower core. The axis for which the summed differences is minimal corresponds to the most likely arrival direction of the primary particle.

Naturally, the expected variance on the reconstructed ϕ and θ diminishes the more stations participate in the combined fit. The angular resolution thus decreases for larger energies of the primary particle. This can be seen in **??**. In any case, the angular
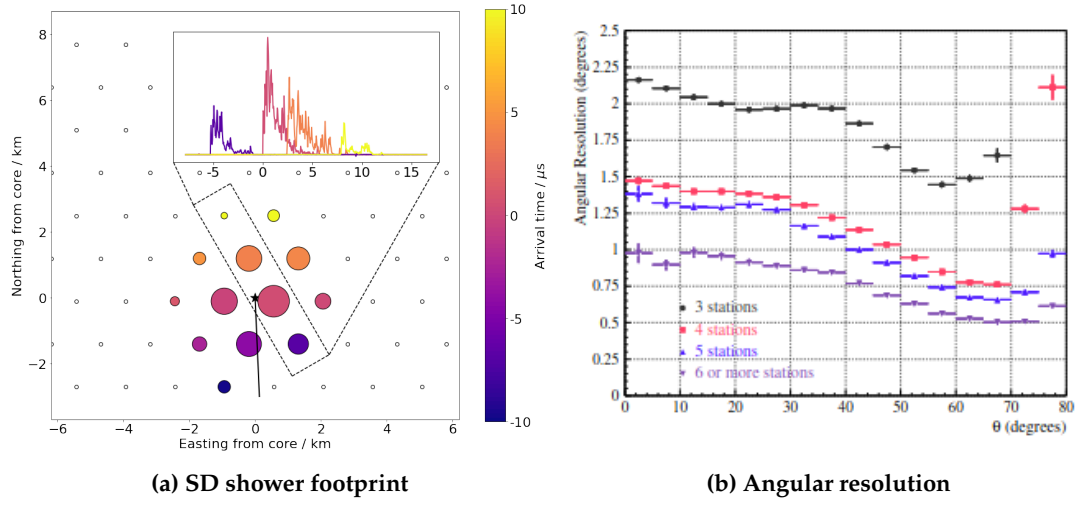
(a) SD shower footprint

(b) Angular resolution

Figure 6: (a) An example shower footprint recorded by the individual SD tanks (circles). The measured signal strength and arrival time is encoded in the size and color for each station. Tanks that haven't recorded any signal are shown colorless. For a subset of stations the respective VEM trace and consequently the propagation of the signal in the SD detector is shown in the inset plot on the top right. **(b)** The angular resolution as a function of θ for energies exceeding 3 EeV. Image from [**bonifazi2005angular**].

resolution even at smaller energies is better than 2.2°. For hybrid events, where the shower has also been detected by the FD, the angular resolution is greatly increased to about 0.6° [**bonifazi2005angular**].

3.4 Energy estimation

After a shower core has been pinpointed and the shower axis was determined, all information to fit an LDF is present. The **S**hower**P**lane **d**istance (SPD), the minimal separation between shower axis and station position, is calculated for each tank participating in the event and related to the integrated signal S (in units of Q_{VEM}) it received. From the so gathered lateral distribution of a shower the integrated signal S_{1000} of a hypothetical (labelled dense) station laying at SPD = 1000 m is obtained. This standardizes the comparison of results across many different events, even if a shower has only triggered few stations [**gaisser1977reliability**].

Due to attenuation effects in the atmosphere S_{1000} is a function of θ. It has been shown in [**DarkoCIC**] that by separating the θ dependence of a signal $S(\theta) = S \cdot A(\theta)$ and normalizing to a reference shower inclination, a reasonably unbiased estimator S_{38} can be recovered via a Constant Intensity Cut (CIC) as shown in **??** and **??**.

$$f_{\text{CIC}} = \frac{S_{1000}(\theta)}{S_{1000}(\theta_{\text{ref}})} = \frac{A(\theta)}{A(\theta_{\text{ref}})}. \tag{5}$$

The reference angle is chosen as $\theta_{\text{ref}} = 38°$, as this is the median inclination of detected events [**aab2020measurement**]. It follows

$$S_{38} = \frac{S_{1000}(\theta)}{f_{\text{CIC}}(\theta)}.$$ (6)

Further corrections are applied to S_{38} in order to counteract influence of the local weather or geomagnetic effects [**aab2020measurement**]. What remains is a shower parameter which has been sanitized as much as possible from any environmental factors, and which has a proportionality to the energy of the primary particle, as discussed in **??**.

The approximate relation of $S_{38}(E)$ can be inferred from hybrid measurements, where the calorimetric energy as measured by the FD is connected to S_{38}. From such datasets it follows the relation below, with the fit parameters for A, B as determined in [**PhysRevD.102.062005**].

$$E_{\text{SD}} = A\,(S_{38}/\,\text{VEM}_{\text{Ch.}})^B$$ (7)

$$A = (1.86 \pm 0.03) \times 10^{17}\,\text{eV}$$
$$B = 1.031 \pm 0.004$$

3.5 Primary particle

The determination of the primary particle, also referred to as the mass composition, relies on the systematic differences in air showers discussed in **??**. Muons, due to their noninteracting nature at high energies are typically the first signal to arrive in a WCD from an air shower. Since high-mass primaries produce a higher fraction of muons this implies that the rise time, in which the integrated signal goes from 10% to 50% of the total received signal, is shorter in these showers. Consequent analysis over a statistically relevant dataset thus reveals the mass composition of the cosmic ray flux (compare [**letessier2014highlights**], **??**)

Neural networks

The idea of a **N**eural **N**etwork (NN) is to attempt to capture the human thinking process in machine code. For this purpose, a network architecture connects some input (e.g. a picture) to an output (e.g. digits 0-9). Much like in a human brain, the architecture consists of multiple smaller chunks, neurons and layers, which connect in some way to form an emergent intelligent system.

As described, neural network do not yet hold the abilities to achieve their designated tasks, and can hardly be called intelligent. They need to be trained. This is done by presenting an example input (called training data) to the network. The network output is compared to the desired output for the given input via some loss function. During training, the network attempts to minimize this loss function. How it is minimized is often a design choice, and in general will depend on the network architecture, which in turn is influenced by the type of data and kind of task the NN should accomplish.

In the following several network architectures which are relevant for this work are detailed. The most simple option of a **D**ense NN (DNN) is given in **??** in order to introduce several key concepts. **C**onvolutional NNs (CNNs) used for example in image recognition are explained in **??**. Lastly **R**ecurrent NNs (RNNs) that find an application in time series analysis are shown in **??**

1 Dense neural network

Dense neural networks are subdivided into layers, which themselve consist of individual neurons. Each neuron conglomerates information from a previous layer according to some weights w_{jk} and a bias b_j and propagates it through some nonlinear activation function $\sigma^{(i)}$. That is, the propagation of an input to the output layer through intermediate, hidden layers $\mathcal{L}^{(i)}$ can be described with the below matrix form:

$$\mathcal{L}_j^{(i)} = \sum_{k=0}^{n^{(i-1)}} \sigma^{(i)} \left(w_{jk} \mathcal{L}_j^{(i-1)} + b_j \right). \tag{1}$$

In **??** $\mathcal{L}_j^{(i)}$ is the value of neuron j in layer i, and $n^{(i)}$ is a reference to the number of neurons in layer i. The activation function achieves two important goals. First, it limits the numerical value neurons can have. This ensures numerical stability during training, and is typically achieved by choosing a sigmoidal activation function. Secondly, the nonlinearity of the activation function ensures that the propagation function of the

entire network cannot mathematically be reduced to a single layer, as this disallows the network to learn nonlinearly separable patterns [**russell2010artificial**].

Important to note is the fact that the usage of one densely connected layer does not restrict the network architecture to consist solely of such layers. In fact, the network architectures discussed here and in the following section can all be used interchangably. This is a common practice in model building [**szegedy2015going**, **krizhevsky2017imagenet**].

2 Convolutional neural network

Convolutional neural networks introduce convolutional layers, which aggregate information from nearby input values. Nearby in this case referring for example to proximate pixels in a 2D image, or neighbouring voxels in a 3D scan. Even succesive inputs in a 1-dimensional time series can be convoluted. In general, the working principle of a convolutional layer can be extended to an arbitrary input shape and size, but will be representatively explained here for a two-dimensional, image-like input.

The convolution in a single layer is done by one or several filters, matrices, that are scalar-multiplied to subchunks of the input data. For example a mock filter like

$$\mathcal{F} = \begin{pmatrix} -1 & -1 & -1 & -1 & -1 & -1 \\ -1 & +1 & -1 & -1 & +1 & -1 \\ -1 & -1 & -1 & -1 & -1 & -1 \\ -1 & +1 & -1 & -1 & +1 & -1 \\ -1 & +1 & +1 & +1 & +1 & -1 \\ -1 & -1 & -1 & -1 & -1 & -1 \end{pmatrix}$$
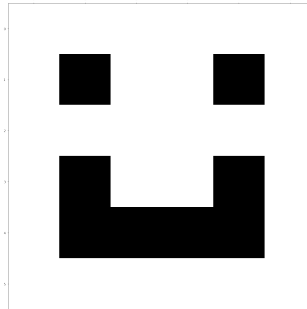
could be swept across an entire image area. During the iteration, areas of the image that resemble the filter will result in a large (relative to the input data) positive scalar value.

In this fashion, an image can be efficiently scanned for specific patterns (lines, edges, etc.) with just few parameters. Namely, these are the numerical values in the filter matrices, which can be optimized during training. The resulting output of a single layer containing different filters can interatively be propagated into subsequent convolutional layers (searching for curves, corners, etc.) until full-scale image detection of complex structures becomes possible.

(a) simple RNN   **(b) LSTM**
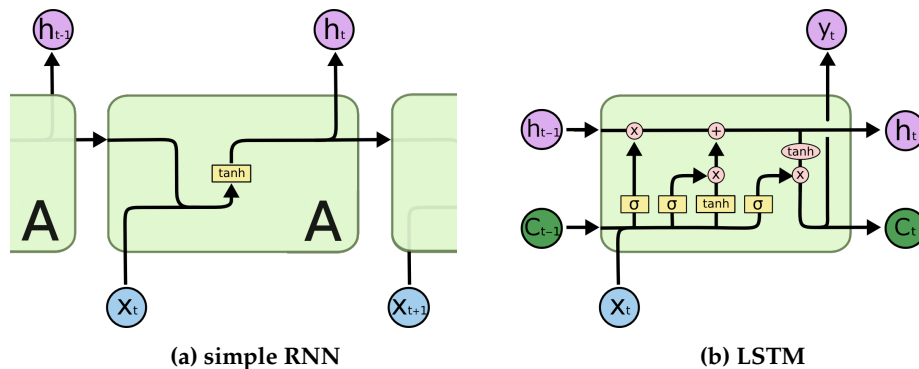
a) An example RNN architecture, with one layer A, where the network output h_t of at step t is used as an additional input for step $t + 1$. Image altered from [**NN-images**].
b) The architecture of a single LSTM layer relies on multiple gates, that update the network configuration, or memory of the layer. From [**NN-images**] with changes. .

3 Recurrent neural network

Recurrent neural networks not only propagate an input value forward through their architecture, but also introduce cyclic connections between distinct layers. For example, in the simplest conceptional case there exists a feedback loop that connects the output of a single network layer to its' input(c.f. **??**). Other feedback configurations are of course possible, and generally preferred, as they can address the problem of vanishing/exploding gradients [**hochreiter1991untersuchungen**].

Moreover, due to the cyclic connections in the network architecture, RNNs are espically qualified for time-series analysis. i.e. where temporally sucessive inputs are highly correlated. A popular example is the **L**ong **S**hort-**T**erm **M**emory (LSTM) architecture, which is visualized in **??**.

The output of a single LSTM layer at timestep $t \neq 0$ is calculated from two variables, the hidden state h_t, as well as the cell state C_t. The former exists in some form in every RNN, while the cell state C_t corresponds to a long-term memory that is unique to the LSTM architecture [**gers2000learning**]. Unlike the name implies, the hidden state corresponds to the output of the network, and is thus in no way hidden. Due to vanishing/exploding gradients, the hidden state does not preserve information for more than few iterations. For this reason, it is often referred to as the short-term memory of the network. Data propagates through an LSTM layer according to the below steps (c.f. as well **??**):

- A sigmoid layer outputs a number between 0 and 1 depending on the input x_t. The cell state from the previous iteration, C_{t-1}, is weighted by this number. In this fashion, the network can choose to discard or keep information from previous iterations. The first sigmoid layer is thus aptly named the forget gate.

- Next, the new cell state is calculated by extracting important information from the input. This is achieved via a feature extraction layer, which is weighted by another instance of a sigmoidal layer. The thus recovered new long term memory

is added to the weighted cell state C_{t-1} and represents the new cell state C_t. This is the input gate of the LSTM.

- Lastly, the hidden state h_t is computed at the output gate of the LSTM. A feature extraction layer processes C_t and provides an output, that is weighted by one last sigmoid layer dependant on the input x_t.

4 Other architectures

With the current rise of deep learning applications in every facet of data processing, a plethora of other architectures have been established to achieve specific tasks. Some of these are purely generative (e.g. **G**enerative **A**dversarial **N**etworks (GANs) [**creswell2018generative**]) or not out of the box suitable for classification due to other reasons. Of particular interest, specifically for this work, are architectures that have been shown to outperform others in time-series analysis. Apart from the LSTM discussed in **??** the **G**ated **R**ecurrent **U**nit (GRU) [**dey2017gate**] is a popular implementation of a recurrent neural network. Last but not least, transformers [**vaswani2017attention**] have consistently been among the most promising architectures for time-series analysis. However, because they require a lot of computational resources they are not compatible with the use-case that this work is pertaining to.